



Photoinduced modification of optical properties of ferroelectric PZT thin films

Saeed Yousefi, Department of Materials Science and Engineering, University of California Davis, Davis, CA 95616, USA

Nelson Hua, Department of Physics, University of California San Diego, La Jolla, CA 92093-0317, USA

Jugal Mehta, and Jianheng Li, Department of Materials Science and Engineering, University of California Davis, Davis, CA 95616, USA

Loïc Guillemot, Center for Nanoscience and Nanotechnology (C2N), UMR CNRS, Paris-Saclay University, 10 Boulevard Thomas Gobert, 91120 Palaiseau, France


Geoffery Rippey, and Louie Zhong, Department of Materials Science and Engineering, University of California Davis, Davis, CA 95616, USA

Richard D. Schaller, Center for Nanoscale Materials, Argonne National Laboratory, Lemont, IL 60439, USA

Thomas Maroutian, Center for Nanoscience and Nanotechnology (C2N), UMR CNRS, Paris-Saclay University, 10 Boulevard Thomas Gobert, 91120 Palaiseau, France

Kristoffer Haldrup, Department of Physics, Technical University of Denmark, Fysikvej, 2800 Kgs. Lyngby, Denmark

Sylvia Matzen, Center for Nanoscience and Nanotechnology (C2N), UMR CNRS, Paris-Saclay University, 10 Boulevard Thomas Gobert, 91120 Palaiseau, France

Roopali Kukreja , Department of Materials Science and Engineering, University of California Davis, Davis, CA 95616, USA

Address all correspondence to Roopali Kukreja at rkukreja@ucdavis.edu

(Received 7 April 2023; accepted 28 August 2023; published online: 25 October 2023)

Abstract

This study investigates ultrafast photoinduced changes in optical properties of ferroelectrics (PZT) on femtosecond to nanosecond timescales, using broadband transient reflectivity studies. Surprisingly, spectral features were observed below the bandgap, which could not be attributed to ground state bleaching, excited state absorption, and/or stimulated emission. A model based on probe energy independent changes in refractive index and extinction coefficient showed good agreement with experimental results. Three relaxation processes were phenomenologically considered for the temporal evolution. Laser-induced heating was ruled out as the cause of short timescale behavior and photorefractive effect was suggested as a potential mechanism for changes in the optical properties.

Introduction

Ferroelectric materials are a class of dielectric materials that possess thermodynamically stable polarization. This electric polarization arises due to the non-centrosymmetric nature of the unit cell of the ferroelectric crystal structure and can be switched by an electric field.^[1] Ferroelectric materials show a wide range of unique properties including ferroelectric hysteresis, high relative permittivity, piezoelectric effect (both direct and inverse), pyroelectric behavior, and strong electro-optic effect. Especially, electro-optic effects whereby optical properties can be modified using electric field is of interest for applications in laser switches, optical shutters, integrated optical/photonics devices and modulators for optical communication. With the development of ferroelectric thin films and heterostructures, novel methods have been established to control polarization and tailor their functional properties. For example, methods such as polarization-strain coupling via epitaxial strain imparted by substrate, or screening of depolarization field by top/bottom layer (usually electrodes) in heterostructures, have been used to control functionalities in thin films.^[2,3] The potential for tunable functional properties also makes ferroelectric thin film and heterostructures of interest for a wide variety of applications including optical sensors, optical mixing, mechanical actuators or resonators for micro-mechanical systems (MEMS).^[4] Additionally, in analogy to

ferromagnetic materials, ferroelectric polarization switching has also been considered for non-volatile memory and data storage applications.^[5]

Recently, ultrafast laser excitation of ferroelectric materials has emerged as an innovative approach to control unique functional properties at femtosecond (fs) to nanosecond (ns) timescales. Specifically, it has been shown that photoinduced excitation and subsequent splitting of electron-hole pairs in ferroelectric materials can result in open-circuit voltages, modification of internal depolarization field, linear photovoltaic effects, optical rectification, and photoinduced structural changes.^[5,6] However, the mechanisms underlying photoinduced behavior in ferroelectrics at ultrafast timescales are not well understood. While a few ultrafast X-ray studies have been performed to investigate structural behavior of ferroelectric thin films,^[2,3,7] photoinduced ultrafast studies of ferroelectric materials to investigate charge carriers behavior or optical response are rare. Photoinduced evolution of charge carriers can dictate the changes in optical properties or even structural behavior via photogenerated shift and screening currents as shown for PbTiO₃ thin films.^[6] As mentioned above, ferroelectric materials show strong (linear) electro-optic effect whereby optical properties including the refractive index can be modified as a function of electric field, i.e., Pockels effect.^[8] Ferroelectric materials also show non-linear optical effect (or photorefractive

effect) which results in change in the refractive index following photoinduced redistribution of electron and holes.^[9] Thus, measuring ultrafast evolution of charge carriers and optical constants including refractive index and absorption coefficient are crucial in order to develop a fundamental understanding of photoinduced behavior in ferroelectric materials.

In this article, we utilized broadband transient reflectivity ($\Delta R/R_0$) measurements on one of the archetypical ferroelectric materials, $\text{Pb}(\text{Zr}_{0.52}\text{Ti}_{0.48})\text{O}_3$ (PZT), to investigate the photoinduced behavior of optical properties. We investigated PZT thin films and heterostructures which are similar to the samples used in previous time-resolved X-ray studies^[7] to directly compare photoinduced evolution of structural and optical response. Furthermore, the PZT heterostructures investigated here are similar to the heterostructure stacks used for ferroelectric devices, and thus, can provide insights into key differences between behavior of thin films vs heterostructures. The experimentally measured broadband transient reflectivity response of PZT thin films and heterostructure was compared with the simulated transient reflectivity calculated using established multilayer thin film reflectivity simulation code.^[10] Based on the transient reflectivity calculations, we show that below band gap $\Delta R/R_0$ spectral features are dominated by photoinduced changes in refractive index (n) and absorption coefficient (k). Photoinduced temporal evolutions for Δn and Δk were then retrieved with the assumption of probe energy independent modification of optical constants. Thermal modeling showed that photoinduced heating was not the dominant effect at shorter picosecond (ps) timescales. We propose that the change of Δn and Δk is due to the photorefractive effect, which modulates the optical constants in the presence of structured light, i.e., spatial modulation of light due to interference effects. As the interference of the pump beam reflected from different interfaces (film/air, film/substrate, film/electrode) in the material can result in the structured light, and the fact that ferroelectrics including PZT show strong Pockels effect, ferroelectrics are prone to show strong photorefractive effect.^[9,11,12] Photorefractive effect thus could drive the modification of refractive index and absorption coefficient, however, additional theoretical studies are required to confirm this mechanism. Our studies highlight the novel routes for ultrafast control of optical properties in ferroelectrics.

Methods

Experimental details

Broadband $\Delta R/R_0$ experiments were performed on PZT thin films with 100 and 200 nm thickness (referred as 100 nm PZT and 200 nm PZT) and ITO(20 nm)/PZT(200 nm)/SrRuO₃(30 nm) heterostructure (referred as ITO/PZT/SRO). PZT films were grown using pulsed laser deposition on SrTiO₃ (STO) substrates. Additional information regarding the PZT thin film samples can be found in the Ref. 7 and in the supplementary information section S1. The optical pump-probe experiments were conducted at the Center for Nanoscale Materials at Argonne National Laboratory using ultrashort laser pulses

with a duration of 50 fs and a repetition rate of 1 kHz. For the optical pump-probe studies, a pump beam with an energy of 3.5 eV (above PZT bandgap ~ 3.3 eV^[13]) was used to excite carrier dynamics in PZT. A broadband white probe beam with an energy range of 1.5–3.5 eV and repetition rate of 2 kHz was used to measure the changes in the optical properties due to the pump pulse. Figure 1(a) shows a schematic of the normal-incidence experimental setup used for optical pump-probe studies. The pump beam was focused to a spot size of 125 μm at the sample resulting in an energy density of 15 mJ/cm². The probe beam had a smaller spot size of 50 μm . Differential reflectivity data were measured by varying the time delay between pump and probe from 0 to 6400 ps. It should be noted that the differential reflectivity signal was normalized to the ground state reflectivity to obtain $\Delta R/R_{0,\text{exp}}$, presented throughout the article.

Reflectivity simulations & analysis

The experimentally measured $\Delta R/R_{0,\text{exp}}$ response was compared with calculated $\Delta R/R_{0,\text{calc}}$ obtained using reflectivity simulations as described below for both the ground state and excited state. As a first step, ground state reflectivity was calculated by considering the reflection of the probe beam from the thin films/heterostructures interfaces. For example, for PZT thin films grown on STO substrate, there are two reflected beams, one from the surface and one from the PZT/STO interface, as shown in Fig. 1(a). The reflection from both interfaces results in an interference pattern which presents as a modulation of the reflected intensity as a function of probe photon energy. The ground state reflectivity depicting the interference pattern is presented in the supplementary information section S2. Note that the oscillatory behavior in the ground state reflectivity is a direct consequence of the interference of the reflected beam from multiple surfaces/interfaces due to acquired phase difference as the beam travels through the sample. Optical constants (refractive index, n and absorption coefficient, k) used in these calculations were either acquired from literature or measured, and are included in the supplementary section S2.^[7,14,15] Note that for the PZT layer, optical constants for $\text{Pb}(\text{Zr}_{0.20}\text{Ti}_{0.80})\text{O}_3$ composition were used due to lack of availability of optical constants in the literature for the $\text{Pb}(\text{Zr}_{0.52}\text{Ti}_{0.48})\text{O}_3$ composition. In the second step, the transient reflectivity signal (measured using the broadband probe beam) following laser excitation was calculated by considering modification of the n and k values.

Ground and transient state (Probe) beam reflectivity of the thin films and heterostructures were calculated using “A Layered Thin Film Transmission and Reflection Coefficient Calculator” Matlab code.^[10] This software calculates the complex reflection and transmission coefficients of a multilayer stack based on the Fresnel equations. This software is based on method described by Pascoe^[16] and we present a brief summary here. The method utilizes characteristic matrices to determine the reflectivity and transmissivity through an arbitrary number of film layers. This method considers that the propagation of plane waves (probe beam) incident on the infinite planar surface (i.e., film) through a

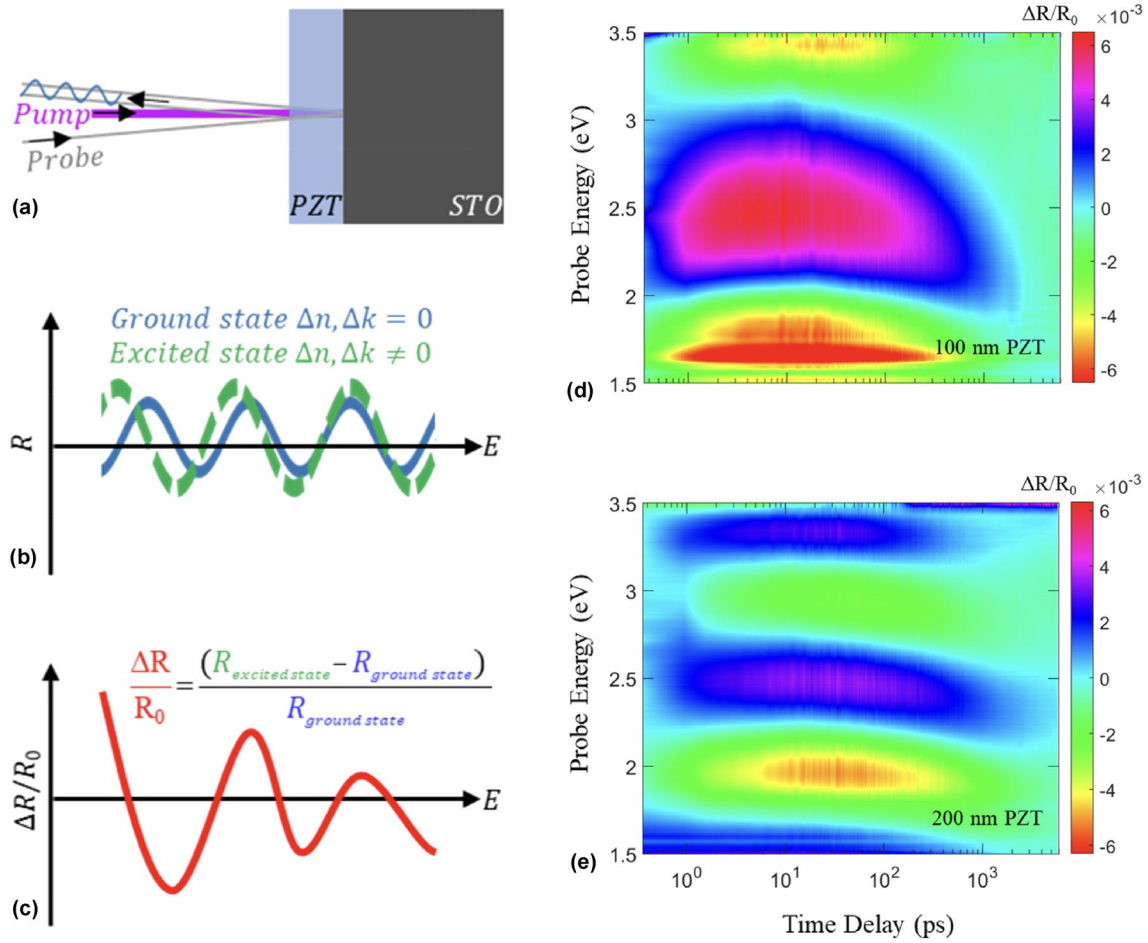


Figure 1. (a) Schematic of pump-probe geometry utilized to measure the photoinduced changes in n and k as a function of time, (b) Schematic illustration of the ground and excited state reflectivity as a function of (probe) photon energy depicting of the interference pattern, and (c) $\Delta R/R_0$ as a function of (probe) photon energy which shows oscillatory behavior due to photoinduced modification of n and k values. Experimentally measured $\Delta R/R_{0, \text{exp}}$ of PZT thin films of (d) 100 nm and (e) 200 nm. The PZT samples were excited using 3.5 eV pump and the reflectivity was measured in the energy range of 1.5–3.5 eV using a broadband probe.

lossless medium (i.e., air) can be described using a set of characteristic matrices which take into account the thickness and material properties of each layer, as well as the incident angle.^[17] As the electromagnetic wave travels from the origin (of the optical system) to a specific point in the sample (i.e., buried interface), characteristic matrix relates the electromagnetic field at this specific point to the one at the origin of the optical system according to the wave propagation theory. The characteristic matrix has been derived by Pascoe^[16] and we only include the final result here,

$$\mathbf{M}_i = \begin{bmatrix} \cos\delta & (i/\eta)\sin\delta \\ (i\eta)\sin\delta & \cos\delta \end{bmatrix}, \quad (1)$$

where M_i is the characteristic matrix of a film layer i , and δ and η are given by $\delta = i\gamma d \cos\theta$ and $\eta = Y \cos\theta$ for transverse electric polarization ($\eta = Y/\cos\theta$ for transverse magnetic polarization). Here, d is the layer thickness and θ is the incident angle. The admittance (inverse

of the impedance) of the film material layer is defined as $Y = \sqrt{(\sigma + i\omega\epsilon)/i\omega\mu}$, where ϵ is the electric permittivity, σ is the conductivity, μ is the magnetic permeability and ω is the frequency. Also, $\cos\theta = \sqrt{1 - (n_{\text{air}}/n \sin(d))^2}$, is a function of complex refractive index (n), refractive index of air (n_{air}) and layer thickness (d). The propagation constant (γ) which includes both the attenuation (real part), and phase changes (imaginary part) is defined as $\gamma = \sqrt{(\sigma + i\omega\epsilon)(i\omega\mu)} = ik_w$, where k_w is the wavenumber and all the other constants are as defined above. Such a characteristic matrix can be defined for each layer, and the total matrix for the whole system is then given by,

$$\mathbf{M}_{\text{total}} = \mathbf{M}_1 \mathbf{M}_2 \mathbf{M}_3 \cdots = \begin{bmatrix} \mathbf{m}_{11} & \mathbf{m}_{12} \\ \mathbf{m}_{21} & \mathbf{m}_{22} \end{bmatrix}, \quad (2)$$

where M_1, M_2 , and M_3 are characteristic matrices for each individual layer and m_{ij} represent the components of the total matrix. The total matrix can be used to obtain the reflection

coefficient (r) and total reflectivity (R) of the total multilayer stack,

$$r = \frac{\eta_1(m_{11} + m_{12}\eta_L) - (m_{21} + m_{22}\eta_L)}{\eta_1(m_{11} + m_{12}\eta_L) + (m_{21} + m_{22}\eta_L)} \quad (3)$$

and reflectivity can be calculated as $R = r^*$. Here, subscripts 1 and L refer to the first and the last (substrate) layers, η and m_{ij} are same as defined above. As the aforementioned parameters ($\epsilon, \sigma, \mu, \dots$) are functions of the optical constants, this method was used to calculate reflectivity throughout the article as a function of n and k (see additional details in supplementary section S2).

In order to calculate the modification of n and k (Δn and Δk), we redefined the calculated transient reflectivity, introduced in the previous section, as a multivariable symbolic function. This function is dependent on parameters such as the probe energy, n and k for each layer, ground state reflectivity, and layers' thicknesses. The fitting variables (Δn and Δk) were added to n and k of the PZT layer. This function was then used to fit the experimental transient reflectivity, at each time delay, using multivariable lsqcurvefit algorithm in Matlab. An assumption that photoinduced changes in n and k are independent of the (probe) photon energy was used for these simulations. Figure 1(b) schematically illustrates both ground state (blue) and excited state (green) reflectivity. Note that the interference patterns exhibiting oscillatory behavior in the excited state will be different compared to the ground state oscillations, due to slight changes in the optical constants. Calculated differential reflectivity, $\Delta R/R_{0,\text{calc}} = (R_{\text{excited-state}} - R_{\text{ground-state}})/R_{\text{ground-state}}$, was then obtained using calculated excited state reflectivity ($R_{\text{excited-state}}$) and calculated ground state reflectivity ($R_{\text{ground-state}}$) as shown in Fig. 1(c). The calculated differential reflectivity, $\Delta R/R_{0,\text{calc}}$, was compared with the experimental result, $\Delta R/R_{0,\text{exp}}$ for both PZT thin films and ITO/PZT/SRO heterostructures. The only difference for the heterostructures sample was that the interference effects due to reflection from four interfaces (surface, ITO/PZT, PZT/SRO, SRO/STO) were considered.

Results

Figure 1(d) and (e) shows experimentally measured broadband probe reflectivity ($\Delta R/R_{0,\text{exp}}$) for PZT thin films (100 and 200 nm) for the energy range of 1.5–3.5 eV, following photoexcitation by the laser pump pulse (3.5 eV, 50 fs). Drastically different spectral features and temporal evolutions are observed for $\Delta R/R_0$ for the two thin films. To understand the experimentally observed spectral features, we calculated $\Delta R/R_{0,\text{calc}}$ by considering modification of optical constants n and k , as described in the previous section. For the clarity of presentation, we first focus on the results obtained for the 200 nm PZT thin film calculations and later expand the calculations for other configurations.

We determined the combination of Δn and Δk required to reproduce the experimentally observed spectral features ($\Delta R/R_{0,\text{exp}}$) at a specific time delay, using the steps laid out in "Methods" section. Figure 2 shows the calculated $\Delta R/R_{0,\text{calc}}$ (red curves) as well as the experimentally measured $\Delta R/R_{0,\text{exp}}$ (black curves), for four different time delays, (a) 0.35 ps, (b) 9.95 ps, (c) 700 ps, and (d) 4000 ps for 200 nm PZT thin film. The red curves show calculated $\Delta R/R_{0,\text{calc}}$ for a) $\Delta n = 7.8 \times 10^{-4}[\pm 8 \times 10^{-5}]$ and $\Delta k = 1.2 \times 10^{-3}[\pm 2 \times 10^{-4}]$, b) $\Delta n = 5.9 \times 10^{-4}[\pm 5 \times 10^{-5}]$ and $\Delta k = 7.2 \times 10^{-3}[\pm 2 \times 10^{-4}]$, c) $\Delta n = -4.2 \times 10^{-4}[\pm 3 \times 10^{-5}]$ and $\Delta k = 3.9 \times 10^{-3}[\pm 4 \times 10^{-4}]$, and (d) $\Delta n = -3.9 \times 10^{-4}[\pm 1 \times 10^{-4}]$ and $\Delta k = 8.6 \times 10^{-4}[\pm 1.5 \times 10^{-4}]$. Additional time slices are shown in supplementary section S3. The comparison of calculated and experimentally measured $\Delta R/R_0$ shows that this approach based on an assumption of energy independent photoinduced changes in n and k can reproduce the key spectral features for all time delays except at the short time delays (i.e., ~ 0.35 ps). Moreover, at longer time delays ($> \sim 4$ ns) the amplitude of the calculated spectral features shows good agreement with the experimental results. The differences between the measured and the calculated dataset for the first ~ 0.35 ps following laser excitation, could be due to other factors which dominate at shorter timescales such as carrier excitation, shift currents and thermal stabilization of carriers.^[2,18] We also note that the amplitude and spectral features of the calculated spectra matched well with the experimental dataset at lower energies, while at higher energies the spectral features are off by about 0.3 eV. This will be further discussed in the "Discussion" section. However, the simple calculations do reproduce key spectral features in $\Delta R/R_0$ as shown in Fig. 2, and thus can be used to compare overall trends of changes in Δn and Δk for PZT thin films and heterostructure.

We can now utilize this framework to obtain the photoinduced evolution of n and k for both PZT thin films and heterostructure. In Fig. 3, we compare the measured, $\Delta R/R_{0,\text{exp}}$, (left plots) and calculated, $\Delta R/R_{0,\text{calc}}$, (right plots) for (a) 100 nm PZT thin film, (b) 200 nm PZT thin film, and (c) ITO/PZT/SRO heterostructure as a function of time delay and probe beam energy. For each sample type $\Delta R/R_{0,\text{calc}}$ was calculated using the reflectivity calculations and fitting the experimental data to obtain the best-fit values for the parameters of Δn and Δk for all time delays, as discussed in the "Methods" section. It can be clearly seen that the overall spectral features observed in the measured data are reproduced well by the calculated $\Delta R/R_{0,\text{calc}}$ for all three samples. This indicates that energy independent changes in n and k (photoinduced Δn and Δk) are sufficient to reproduce these spectral features in the simulated data, and modifications in optical constants due to ground state bleaching, excited state absorption, and stimulated emission, are not needed to explain the spectral features of the broadband $\Delta R/R_0$. Previously, for a system photoexcited with a photon energy above the bandgap, the variations in spectral features have been attributed to ground state bleaching for near bandgap energies, excited state absorption for below bandgap energies, and stimulated emission at the bandgap energy.^[19] Since

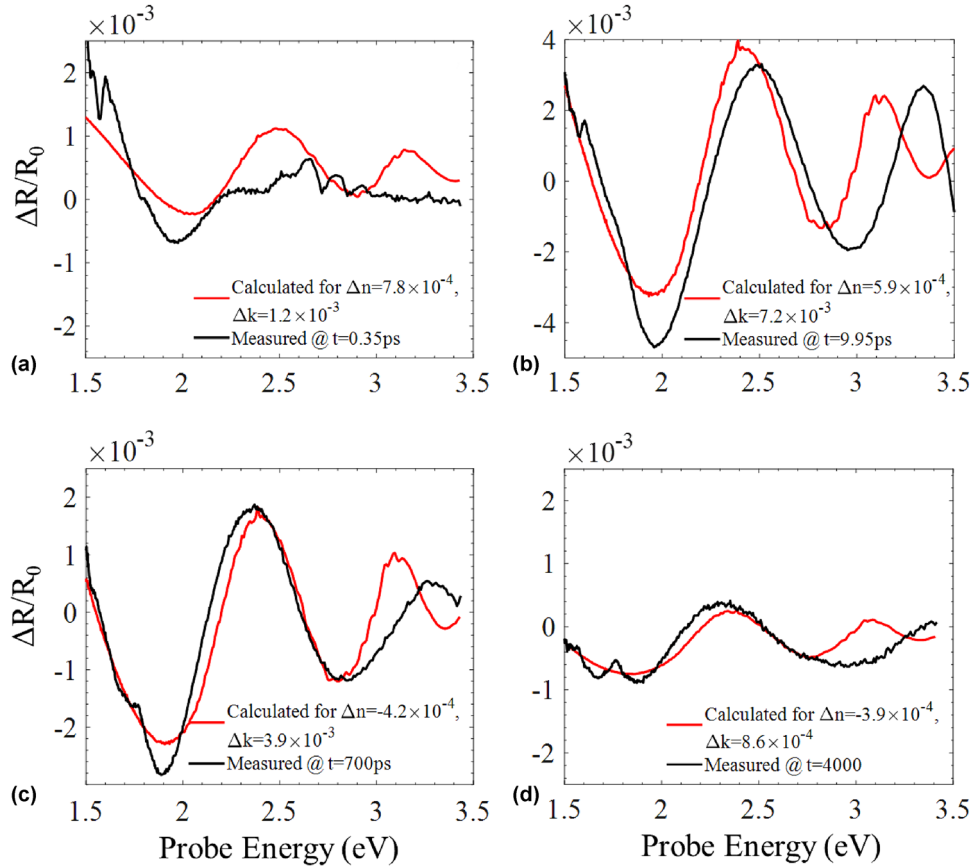


Figure 2. Measured $\Delta R/R_0$ (black) is compared with calculated $\Delta R/R_0$ (red) for 200 nm PZT at time delay of (a) 0.35 ps, (b) 9.95 ps (c) 700 ps and (d) 4000 ps after laser excitation. The respective Δn and Δk for each plot are (a) $\Delta n = 7.8 \times 10^{-4}$ and $\Delta k = 1.2 \times 10^{-3}$, (b) $\Delta n = 5.9 \times 10^{-4}$ and $\Delta k = 7.2 \times 10^{-3}$, (c) $\Delta n = -4.2 \times 10^{-4}$ and $\Delta k = 3.9 \times 10^{-4}$, and (d) $\Delta n = -3.9 \times 10^{-4}$ and $\Delta k = 8.6 \times 10^{-4}$.

the PZT bandgap is around 3.3 eV, the oscillatory spectral features observed below 3.3 eV (i.e., below band gap) imply that we can further rule out the aforementioned reasons.

From the results shown in Fig. 3, we can retrieve the photoinduced changes in n and k , i.e., Δn and Δk , as a function of time for the entire delay range. Figure 4 presents the photoinduced changes in Δn [Fig. 4(a), (b)] and Δk [Fig. 4(d), (e)] as a function of delay for all three samples, 100 nm PZT (black), 200 nm PZT (red), and ITO/PZT/SRO (blue) heterostructure. The supplementary section S4 presents the same datasets in logarithmic scale for clarity. The evolution of Δn and Δk were then fitted using exponential temporal fits which included three exponentials (Eq. 4) to capture fast recovery, medium recovery, and slow recovery. Fits using different decay components, i.e., two or four exponentials were also performed, but ultimately three exponentials were used as they resulted in best fit to the data with the lowest number of degrees of freedom in the fit (see supplementary Section S5 for comparison between multiple decay components). The three exponential decay model used to fit the dynamics is given by the following equation,

$$\Delta n, \Delta k = \sum_{i=1}^3 \frac{1}{2} A_i \left[1 + \operatorname{erf} \left(\frac{t}{\tau_r} \right) \right] \exp \left(\frac{-t}{\tau_{d_i}} \right) \quad (4)$$

where, τ_r is rise time constant for the error function, A_i is the amplitude, and τ_{d_i} is the decay time constant of each component, respectively. The fitting parameters including $A_1, A_2, A_3, \tau_{d1}, \tau_{d2}$, and τ_{d3} are presented in Table S1.

The obtained decay timescales for the temporal evolution for both Δn and Δk show a fast relaxation (τ_{fast}) process within 10's of ps followed by a slower recovery process (τ_{medium}) on timescale of 100's of ps and finally, a longer recovery process over (τ_{slow}) 5–20 ns. It should be noted that the $\Delta R/R_0, \text{calc}$ calculations shown in Figs. 2 and 3 do not simulate the excitation process, and only capture the recovery processes. Furthermore, the experiments only captured 6 ns delay range which results in significant error bars for the slow recovery (τ_{slow}). Comparing different samples, Fig. 4(a), (b), (d), and (e) and Table S1 shows that the relaxation dynamics of Δn is comparable for thin films and heterostructures, albeit slightly different amplitudes. On the other hand, the evolution of Δk is drastically different for thin films and heterostructure, especially the amplitudes (A_1 and A_2) are almost an order of magnitude smaller for the heterostructure. This could be due to lower absorption in PZT due to presence of top ITO layer in the heterostructures, as the presence of ITO attenuates the beam intensity in the PZT layer

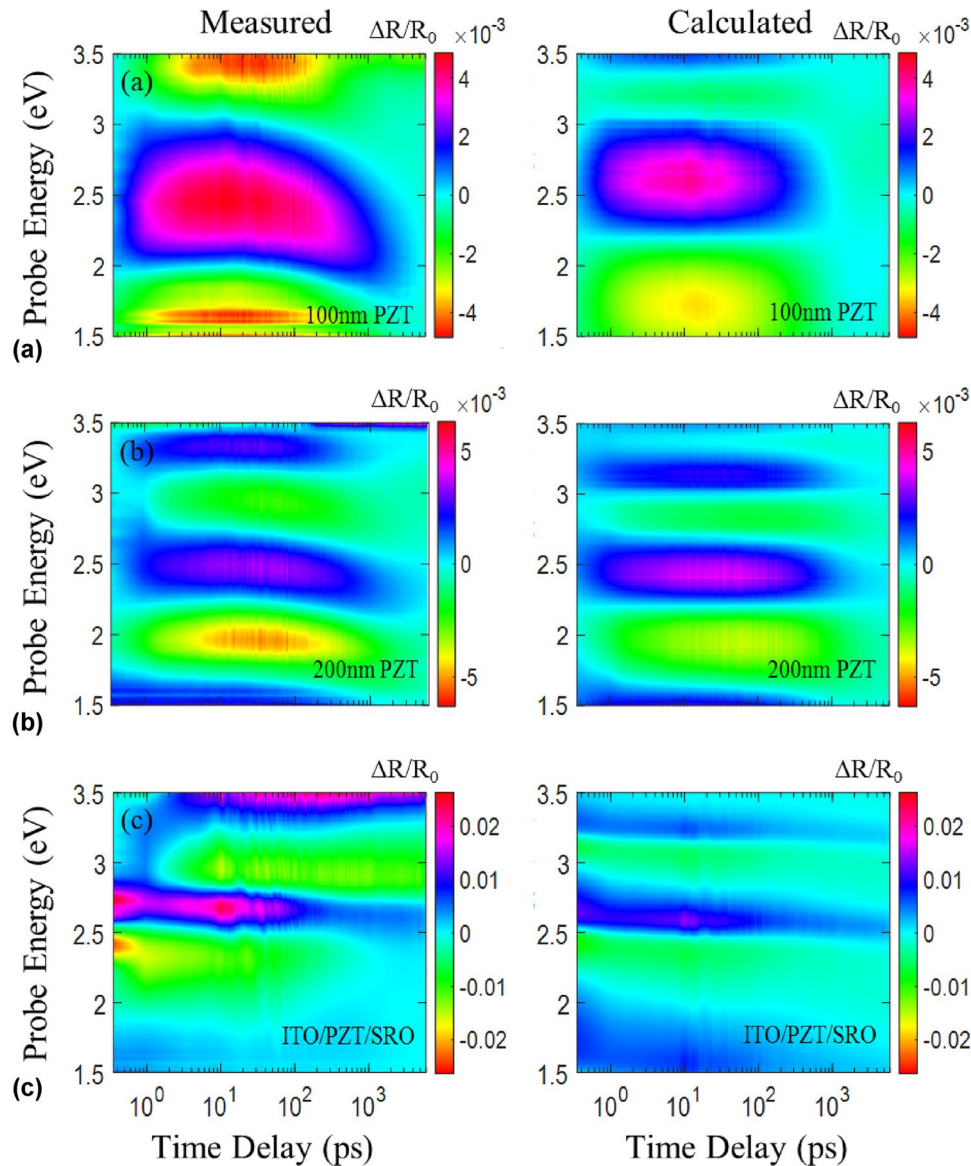


Figure 3. Measured, $\Delta R/R_0, \text{exp}$ (left) and calculated (right), $\Delta R/R_0, \text{calc}$ broadband differential reflectivity for (a) 100 nm PZT thin film, (b) 200 nm PZT thin film, and (c) ITO/PZT/SRO heterostructure.

(Figure S10 in supplementary section S6 shows that ITO layers attenuates the intensity by 30%). Moreover, the presence of a higher number of interfaces results in higher reflection and subsequently, stronger interference effects which can result in larger variation of Δn compared to Δk . Overall, for all three samples, we also find that the recovery time constants are faster for Δn compared to Δk . Additional time-resolved studies are required to confirm such a behavior for other ferroelectric systems. We also note that during recovery, Δn (for both PZT thin films) and Δk (for 100 nm PZT thin film) show a sign reversal and overshoot the ground state value. While the origin for the sign reversal is not clear, recent studies on multiferroic BiFeO₃ have indicated that decrease in the band gap at higher temperatures can result in excess energy of photoexcited carriers.^[18,19]

The photoexcited carriers with excessive energy will undergo electron–phonon scattering and transfer their energy to the phonon degree of freedom. It is then possible that excitation of phonon system results in establishment of a new quasi-equilibrium which manifests itself as a sign reversal in Δn and Δk . Significant variation in optical constants which are forbidden in equilibrium crystal structure have also been recently proposed for SrTiO₃ driven by resonant excitation of Raman phonons.^[20]

In order to clarify the role of laser-induced heating in the recovery processes for Δn and Δk , we simulated the changes in optical constants (n and k) due to heating of the lattice from the absorbed laser power. The increase in the temperature of the film immediately after the excitation was estimated using one-dimensional thermal diffusion equation for heterostructures as

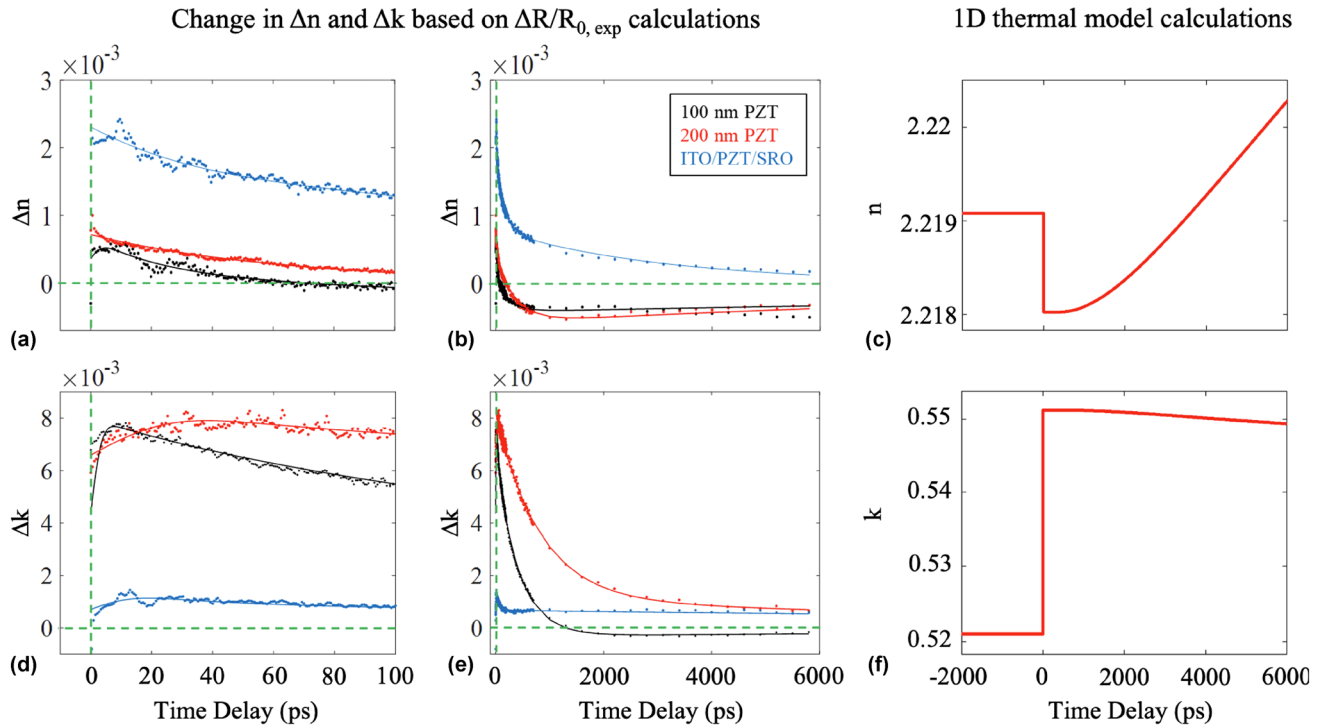


Figure 4. The corresponding amount of change in (a, b) Δn and (d, e) Δk based on $\Delta R/R_0$ calculations of 100 nm PZT (black), 200 nm PZT (red), and ITO/PZT/SRO thin films at different time delays, fitted with three exponential decay models. While Δn follows a similar behavior specifically for 100 nm PZT and 200 nm PZT, Δk is drastically different for the same two films. Calculated temporal evolution of (c) n , and (f) k , obtained by only considering laser-induced heating. Slow relaxation behavior over ns ($> 1-2$ ns) is observed for both Δk and Δn which does not match the fast recovery observed experimentally.

described in detail in the supplementary section S7. Figure 4(c) and (f) plot the temporal evolution of n and k due to laser-induced lattice heating, respectively. Note that increase in n beyond the ground state value at the later timescales [around ~ 4 ns in Fig. 4(c)] is due to non-monotonous temperature dependence of n as shown in Figure S11. Comparing the laser-induced heating behavior [Fig. 4(c) and (f)] with the photoinduced modification for Δn and Δk [Fig. 4(a), (b), (d), and (e)], we see that the evolution at short time delays is quite different with much faster recovery (τ_{fast} and τ_{medium}) than observed for laser-induced heating. Moreover, only the slow recovery time constant ($\tau_{3, \text{slow}}$) is consistent with the timescales obtained from the thermal model. For example, following laser excitation, Δk undergoes a slow relaxation over delay range of 6 ns with an amplitude of $\sim 2 \times 10^{-3}$ [Fig. 4(f)] based on the thermal transport model, which is comparable to $A_3 = 1.5 \times 10^{-3}$ (for Δk for 200 nm PZT) obtained from the temporal exponential fit to the results shown in Fig. 4(e). For Δn , we note that while the slow recovery amplitude, A_3 , does not match the thermal model, the slow recovery time constant ($\tau_{3, \text{slow}}$) is consistent with the thermal model. The discrepancies in the amplitude could be potentially due to radiative recombination of charge carriers which is not considered in our model. Thus, we conclude that behavior at short time scales cannot be explained due to laser-induced heating of the lattice and discuss potential mechanism in the following section.

Discussion

Immediately following laser excitation, the energy is deposited within the electronic system exciting it far from the equilibrium. Even during relaxation and recovery process, as electron-phonon coupling results in transfer of energy to the phonon degrees of freedom, the excited phonon population could be far from thermal in 10–100's ps regime, resulting in both electron and phonon systems in a highly non-equilibrium state.^[21] Photoinduced lattice deformation due to photogenerated charge carriers could be a possible mechanism for photoinduced modification of n and k , but the experimentally measured timescales for structural recovery are within 2–22 ns (for both BaTiO_3 ,^[3] and PZT ^[7]), which are much slower than the timescales observed here. While ps structural recovery has been observed using fs X-rays for PbTiO_3 ,^[2] structural data at such short timescales are currently not available for PZT thin films to conclusively confirm the role of photoinduced lattice deformation.

Another potential mechanism driving modification of optical constants could be due to photogenerated free-carrier and associated charge carrier dynamics leading to photorefractive effect in the PZT thin film. Recently, in halide perovskites, as well as in $\text{Ba}_{0.875}(\text{Bi}_{0.5}\text{Li}_{0.5})_{0.125}\text{TiO}_3$, laser modification of optical constants have been reported,^[22–25] and was attributed to change in internal field distribution driven by photoinduced excitation

of charge carriers and trapped charges.^[25] For ferroelectrics, application of an electric field can modify the optical properties (i.e., Pockels effect^[9]) due to the non-centrosymmetric nature of their crystal structure, increased ionic distortions, and dielectric screening.^[8,26] Ferroelectric materials also show strong photorefractive effect, which is a non-linear effect whereby the required electric field is generated by spatially structured light.^[6,9,11] Typically, spatially structured light is generated by designing experimental optics in a specific manner which results in interference of the incident light on the sample. In our case, light interference can occur due to presence of multiple interfaces in thin films and heterostructure (PZT/air, PZT/ITO, PZT/SRO, PZT/substrate etc.) which will result in multiple reflections of the incident pump and the probe beam. This interference between the beams will result in spatially structured light within the material, which can be calculated using methods described in Refs. 9, 24, 27 and is directly related to the geometry of the heterostructure. Presence of such a spatially structured light within the sample will result in regions which have stronger or weaker electromagnetic field (due to constructive and destructive interference). This difference in the applied electromagnetic field can drive charge redistribution, which in turn will generate a space charge electric field within the material. Consequently, such an electric field generated due to structured light can modify the optical properties of the material (via Pockels effect) immediately following laser excitation.^[23,24,28] On the ps timescales, as the charge carrier populations decay due to carrier recombination,^[3] electron–phonon scattering etc. it will lead to relaxation back to the ground state, resulting in the observed fast recovery of optical properties, Δn and Δk . Moreover, since the interference effects will depend on the geometry of the heterostructures, i.e., interfaces present, it is possible that the differences observed in ultrafast evolution of Δn and Δk for thin film vs heterostructure is then indeed due to photorefractive effect.

Our pump-broadband probe measurements and the reflectivity simulations thus highlight photoinduced modification of Δn and Δk following laser excitation in ferroelectric PZT system. While detailed broadband studies on other ferroelectrics are not yet available, our studies show that careful analysis and interpretation of optical data is needed, especially for pump–(single frequency) probe studies of thin films and heterostructures. We also developed a simple model based on the probe energy independent modification of Δn and Δk which can be also extended to other ferroelectric thin films and heterostructures. This simple model captures the lower probe region of the measured broadband spectrum. The mismatch at higher energies could be due to variety of different factors which if accounted, could further improve these calculations. First, as mentioned before, PZT optical constants were measured for $\text{Pb}(\text{Zr}_{0.20}\text{Ti}_{0.80})\text{O}_3$, while the $\Delta R/R_0$ experiments were performed on $\text{Pb}(\text{Zr}_{0.52}\text{Ti}_{0.48})\text{O}_3$ systems. Second, bulk optical constants^[14,15] were used for SRO and ITO for ITO/PZT/SRO heterostructure calculations due to lack of thin film optical constants in the literature.

Third, the optical constants were extrapolated at the spectrum extremes (above 2 eV), due to lack of static optical constants for the spectrum extremes in the literature. Most importantly, these calculations were performed using the assumption that change in optical constants is independent of energy, i.e., same throughout the spectrum. For more accurate calculation, a probe energy dependent term affecting the photoinduced changes in n and k might need to be considered. Additional theoretical and broadband experimental studies are needed to clarify the energy dependence of the modification in optical constants. These additions can potentially improve the model developed here and bridge the calculated and measured $\Delta R/R_0$ differences at higher energies (above 3 eV).

Conclusions

Photoinduced dynamics of modification of n and k in broadband $\Delta R/R_0$ were investigated for ferroelectric thin films and heterostructure of PZT and ITO/PZT/SRO grown on STO substrates. The experimentally observed changes in spectral features, below band gap, were simulated using a simple model based on energy independent changes in n and k following photoexcitation. Reflectivity calculations obtained using this model corroborated well with the experimentally measured results for all the ferroelectric samples below ~ 3 eV. Phenomenological modeling of the photoinduced changes in n and k indicated that relaxation processes are dictated by fast, medium and slow recovery. Thermal transport model was developed which showed that while lattice induced heating cannot explain fast and medium recovery. Photorefractive effect due to photogenerated charge redistribution was discussed as a potential mechanism to explain the observed changes in optical properties. The differences between the observed optical evolution of thin films and heterostructure indicate that interfacial tailoring can be used to control ultrafast optical behavior. Our pump-broadband probe study thus provides potential routes for achieving desired ultrafast optical properties by carefully designing the ferroelectric heterostructures which could be important for applications in electro-optic modulators or sensors and ultrafast switches.

Acknowledgments

The work at UC Davis was supported by National Science Foundation (DMR-1902652). Research at the Center for Nanoscience and Nanotechnology was supported by the French RENATECH network and by the French National Research Agency (ANR) – Project UP-DOWN (Project No. ANR-18-CE09-0026–04). Work performed at the Center for Nanoscale Materials, a U.S. Department of Energy Office of Science User Facility, was supported by the U.S. DOE, Office of Basic Energy Sciences, under Contract No. DE-AC02-06CH11357.

Data availability

The data can be made available on reasonable request.

Declarations

Conflict of interest

On behalf of all authors, the corresponding author states that there is no conflict of interest.

Supplementary Information

The online version contains supplementary material available at <https://doi.org/10.1557/s43579-023-00476-6>.

Open Access

This article is licensed under a Creative Commons Attribution 4.0 International License, which permits use, sharing, adaptation, distribution and reproduction in any medium or format, as long as you give appropriate credit to the original author(s) and the source, provide a link to the Creative Commons licence, and indicate if changes were made. The images or other third party material in this article are included in the article's Creative Commons licence, unless indicated otherwise in a credit line to the material. If material is not included in the article's Creative Commons licence and your intended use is not permitted by statutory regulation or exceeds the permitted use, you will need to obtain permission directly from the copyright holder. To view a copy of this licence, visit <http://creativecommons.org/licenses/by/4.0/>.

References

- R.E. Cohen, Origin of ferroelectricity in perovskite oxides. *Nature* **358**, 136 (1992)
- D. Daranciang et al., Ultrafast photovoltaic response in ferroelectric nanolayers. *Phys. Rev. Lett.* **108**, 087601 (2012)
- H. Wen et al., Electronic origin of ultrafast photoinduced strain in BiFeO₃. *Phys. Rev. Lett.* **110**, 037601 (2013)
- P. Murali, Ferroelectric thin films for micro-sensors and actuators: a review. *J. Micromech. Microeng.* **10**, 136 (2000)
- L.W. Martin, A.M. Rappe, Thin-film ferroelectric materials and their applications. *Nat. Rev. Mater.* **2**, 2 (2017). <https://doi.org/10.1038/natrevmats.2016.87>
- C. Gu and P. Yeh, in *Photorefractive Materials, Effects, and Applications*, by V.L. Brudny, S.A. Ledesma, M.C. Marconi (Tandil, Argentina, 2001), pp. 9–13.
- S. Matzen et al., Tuning ultrafast photoinduced strain in ferroelectric-based devices. *Adv. Electron. Mater.* **5**, 1800709 (2019)
- E. Efrati, Strong pockels materials. *Nat. Mater.* **18**, 2 (2019)
- P. Günter, J.-P. Huignard (eds.), *Photorefractive Materials and Their Applications 1: Basic Effects* (Springer, New York, 2006)
- Jreftran, A layered thin film transmission and reflection coefficient calculator, <https://www.mathworks.com/matlabcentral/fileexchange/50923-jreftran-a-layered-thin-film-transmission-and-reflection-coefficient-calculator>
- M. Reynaud et al., Electro-optic response in epitaxially stabilized orthorhombic Mm2 BaTiO₃. *Phys. Rev. Mater.* **5**, 035201 (2021)
- J. Nordlander et al., Ferroelectric domain architecture and poling of BaTiO₃ on Si. *Phys. Rev. Mater.* **4**, 034406 (2020)
- S. Samanta, V. Sankaranarayanan, K. Sethupathi, Band gap, piezoelectricity and temperature dependence of differential permittivity and energy storage density of PZT with different Zr/Ti ratios. *Vacuum* **156**, 456 (2018)
- R.A. Synowicki, Spectroscopic ellipsometry characterization of indium tin oxide film microstructure and optical constants. *Thin Solid Films* **313–314**, 394 (1998)
- R.B. Wilson, B.A. Appgar, L.W. Martin, D.G. Cahill, Thermoreflectance of metal transducers for optical pump-probe studies of thermal properties. *Opt. Express* **20**, 28829 (2012)
- K. J. Pascoe, *Reflectivity and Transmissivity Through Layered, Lossy Media: A User-Friendly Approach* (Dayt. OH Air Force Inst. Technol. Wright-Patterson Air Force Base, 2012).
- R.A. Craig, Method for analysis of the characteristic matrix in optical systems. *J. Opt. Soc. Am. A* **4**, 1092 (1987)
- H. Wen et al., Structural and electronic recovery pathways of a photoexcited ultrathin VO₂ film. *Phys. Rev. B* **88**, 165424 (2013)
- R. Berera, R. van Grondelle, J.T.M. Kennis, Ultrafast transient absorption spectroscopy: principles and application to photosynthetic systems. *Photosynth. Res.* **101**, 105 (2009)
- G. Khalsa, N.A. Benedek, J. Moses, Ultrafast control of material optical properties via the infrared resonant Raman effect. *Phys. Rev. X* **11**, 021067 (2021)
- S. de Jong et al., Speed limit of the insulator-metal transition in magnetite. *Nat. Mater.* **12**, 882 (2013)
- Z.G. Yu, S. Krishnamurthy, S. Guha, Photoexcited-carrier-induced refractive index change in small bandgap semiconductors. *J. Opt. Soc. Am. B* **23**, 2356 (2006)
- T. Ghosh, S. Aharon, A. Shpatz, L. Etgar, S. Ruhman, Reflectivity effects on pump-probe spectra of lead halide perovskites: comparing thin films versus nanocrystals. *ACS Nano* **12**, 5719 (2018)
- H.P. Pasanen, P. Vivo, L. Canil, A. Abate, N. Tkachenko, Refractive index change dominates the transient absorption response of metal halide perovskite thin films in the near infrared. *Phys. Chem. Chem. Phys.* **21**, 14663 (2019)
- S. Pal, A.B. Swain, P.P. Biswas, P. Murugavel, Photoferroelectric phenomena in ferroelectric oxides and a Rayleigh analysis. *Phys. Rev. Mater.* **4**, 064415 (2020)
- S. Abel et al., Large Pockels effect in micro- and nanostructured barium Titanate integrated on silicon. *Nat. Mater.* **18**, 42 (2019)
- M.B. Price, J. Butkus, T.C. Jellicoe, A. Sadhanala, A. Briane, J.E. Halpert, K. Broch, J.M. Hodgkiss, R.H. Friend, F. Deschler, Hot-carrier cooling and photoinduced refractive index changes in organic-inorganic lead halide perovskites. *Nat. Commun.* **6**, 8420 (2015)
- R.R. Tamming, J. Butkus, M.B. Price, P. Vashishtha, S.K.K. Prasad, J.E. Halpert, K. Chen, J.M. Hodgkiss, Ultrafast spectrally resolved photoinduced complex refractive index changes in CsPbBr₃ perovskites. *ACS Photon.* **6**, 345 (2019)

Publisher's Note Springer Nature remains neutral with regard to jurisdictional claims in published maps and institutional affiliations.